Ubiquitous lognormal distribution of neuron densities across mammalian cerebral cortex

Aitor Morales-Gregorio[1,2*†], **Alexander van Meegen**[1,2†], **Sacha J. van Albada**[1,2]

***For correspondence:** a.morales-gregorio@fz-juelich.com

[†]These authors contributed equally to this work

[1]Institute of Neuroscience and Medicine (INM-6) and Institute for Advanced Simulation (IAS-6) and JARA-Institut Brain Structure-Function Relationships (INM-10), Jülich Research Centre, Jülich, Germany; [2]Institute of Zoology, University of Cologne, Cologne, Germany

Abstract Numbers of neurons and their spatial variation are fundamental organizational features of the brain. Despite the large corpus of cytoarchitectonic data available in the literature, the statistical distributions of neuron densities within and across brain areas remain largely uncharacterized. Here, we show that neuron densities are compatible with a lognormal distribution across cortical areas in several mammalian species, and find that this also holds true within cortical areas. A minimal model of noisy cell division, in combination with distributed proliferation times, can account for the coexistence of lognormal distributions within and across cortical areas. Our findings uncover a new organizational principle of cortical cytoarchitecture: the ubiquitous lognormal distribution of neuron densities, which adds to a long list of lognormal variables in the brain.

Introduction

Neurons are not uniformly distributed across the cerebral cortex; their density varies strongly across areas and layers (***Brodmann, 1909***; ***von Economo et al., 2008***). The neuron density directly affects short-range as well as long-range neuronal connectivity (***Braitenberg and Schüz, 1991***; ***Ercsey-Ravasz et al., 2013***). Elucidating the distribution of neuron densities across the brain therefore provides insight into its connectivity structure and, ultimately, cognitive function. Additionally, statistical distributions are essential for the construction of computational network models, which rely on predictive relationships and organizational principles where the experimental data are missing (***Hilgetag et al., 2019***; ***van Albada et al., 2022***). Previous quantitative studies have provided reliable estimates for cell densities across the cerebral cortex of rodents (***Herculano-Houzel et al., 2013***; ***Erö et al., 2018***; ***Charvet et al., 2015***), non-human primates (***Charvet et al., 2015***; ***Atapour et al., 2019***; ***Beul and Hilgetag, 2019***; ***Collins et al., 2010***, ***2016***; ***Turner et al., 2016***), large carnivores (***Jardim-Messeder et al., 2017***), and humans (***von Bartheld et al., 2016***; ***von Economo et al., 2008***). However, to the best of our knowledge, the univariate distribution of neuron densities across and within cortical areas has not yet been statistically characterized. Instead, most studies focus on qualitative and quantitative comparisons across species, areas, or cortical layers. Capturing the entire distribution is necessary because long-tailed, highly skewed distributions are prevalent in the brain (***Buzsáki and Mizuseki, 2014***) and invalidate the intuition—guided by the central limit theorem—that the vast majority of values are in a small region of a few standard deviations around the mean.

Here, we characterize the distribution of neuron densities ρ across mammalian cerebral cortex. Based on the sample histograms (***Figure 1***) we hypothesize that ρ follows a lognormal distribution, similar to many other neuroanatomical and physiological variables (***Buzsáki and Mizuseki, 2014***) such as synaptic strengths (***Robinson et al., 2021***), synapse sizes (***Loewenstein et al., 2011***; ***Santuy et al., 2018***; ***Dorkenwald et al., 2022***), axonal widths (***Wang et al., 2008***; ***Liewald et al., 2014***), and cortico-cortical connection densities (***Markov et al., 2014***; ***Gămănuţ et al., 2018***). We used neuron density data from mouse (*Mus musculus*), marmoset (*Callithrix jacchus*), macaque (*Macaca mulatta*), human (*Homo sapiens*), galago (*Otolemur garnettii*), owl monkey (*Aotus nancymaae*), and baboon (*Papio cynocephalus anubis*) to test this hypothesis (see Cell density data for a detailed description of the data). The marmoset, galago, owl monkey, baboon, and macaque$_2$ data sets are based on a single subject; the mouse, macaque$_1$, and human data sets are based on a combination of data across several subjects. The statistical tests conclude that the hypothesis cannot be rejected in the majority of cases, suggesting that the underlying distribution is compatible with a lognormal distribution if the samples are based either on cytoarchitectonically defined areas or on uniformly sampled regions. Beyond the distribution across cortical areas, we show that neuron densities within most areas of marmoset cortex are also compatible with a lognormal distribution. To complement the statistical tests, we perform a model comparison with several other distributions and find that none outperform the lognormal distribution as a model of the data within and across areas. Finally, we show that the lognormal distribution within cortical areas can emerge during neurogenesis from a simple cell division model with variability. The model can furthermore account quantitatively for the lognormal density distribution across areas based on an inferred distribution of proliferation times of the areas. Additional between-area variability in the proliferation rates is also compatible with the model but not necessary to obtain a quantitative agreement with the observed distribution. Thus, our model shows how the lognormal distribution of neurons could emerge both within and across cortical areas.

Results

Lognormal distribution of neurons across cortical areas

To test for lognormality, we take the natural logarithm, $\ln(\rho)$, which converts lognormally distributed samples into normally distributed samples (***Figure 1***B). We then test for normality of $\ln(\rho)$ using the Shapiro-Wilk (SW) test, the most powerful among a number of commonly applied normality tests (***Razali and Yap, 2011***). Large outliers (|z-scored $\ln(\rho)| \geq 3$; marked with a red cross in ***Figure 1***C) were excluded from the normality test. The removed outliers are area $\mathrm{V1}$ in macaque and marmoset, which have densities far outside the range for all other areas in both species, and area APir in marmoset, which has a noticeably distinct cytoarchitecture with respect to the rest of the cerebral cortex (***Atapour et al., 2019***). We denote different data sets for the same species with subscript indices (see Cell density data). The SW test concludes that the normality hypothesis of $\ln(\rho)$ cannot be rejected for mouse, marmoset, macaque$_1$, human, galago$_1$, owl monkey, and baboon (see ***Figure 1***B). For the data sets macaque$_2$ and galago$_2$ the normality hypothesis is rejected ($p < 0.05$); however, in these data sets, the densities were sampled neither uniformly nor based on a cytoarchitectonic parcellation. The normality hypothesis for the distribution across cytoarchitectonic areas is further supported by ***Figure 1***C, which shows that the relation between theoretical quantiles and ordered samples is almost perfectly linear except for macaque$_2$ and galago$_2$.

Next, we test the z-scored $\ln(\rho)$ from the different species and data sets against each other and find that they are pairwise statistically indistinguishable ($\alpha = 0.05$ level; two-sample two-sided Kolmogorov-Smirnov test, see ***Figure 1-Figure supplement 1*** for full test results).

Additionally, we control for cell types in the distributions of the mouse, galago$_1$, owl monkey, and baboon data. In the mouse data, different types of neurons and glia were labeled with specific genetic markers and their respective densities were reported separately for all cell types (***Erö et al., 2018***). In the galago$_1$, owl monkey, and baboon data sets, the total numbers of cells and neurons

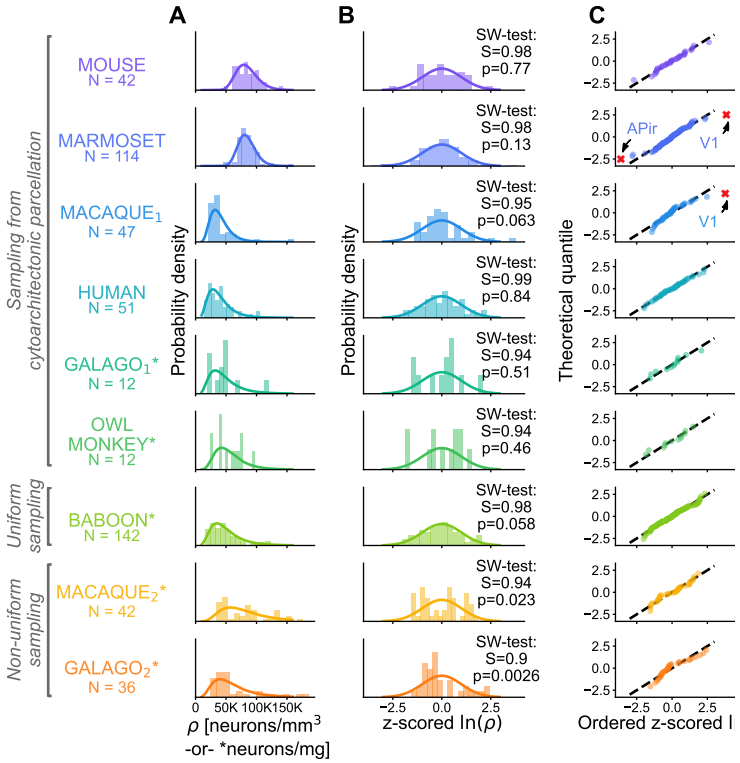

Figure 1. Neuron and cell densities ρ follow a lognormal distribution across cortical areas for multiple species. A Histogram of ρ (bars) and probability density function of a fitted lognormal distribution (line). The number of samples N is either the number of sampled cytoarchitectonic areas (mouse, marmoset, macaque$_1$, human, galago$_1$, and owl monkey) or the number of sampling frames (baboon, macaque$_1$, and galago$_2$). For marmoset, galago, owl monkey, baboon, and macaque$_2$ the data is based on a single subject; for mouse, macaque$_1$, and human it is based on a combination of data across several subjects. **B** Z-scored $\ln(\rho)$ histogram (bars), standard normal distribution (line), and result of the Shapiro-Wilk normality test. **C** Probability plot of z-scored $\ln(\rho)$. Discarded outliers marked with a red cross.

were reported separately (***Collins et al., 2010***). We show that the neuron density distributions for all subtypes of neurons in the mouse are compatible with a lognormal distribution (***Figure 1-Figure supplement 2***; SW test on $\ln(\rho)$, $p > 0.05$) while glia are not—with the notable exception of oligodendrocytes. When neurons and glia are pooled together (***Figure 1-Figure supplement 2***C,D), the distribution of $\ln(\rho)$ still passes the SW normality test, likely due to the distribution being dominated by the neurons. Similar observations are made in the baboon data, where the glia do not pass the lognormality test, but the neurons do. In the cases of galago$_1$ and owl monkey both the neurons and glia pass the lognormality test (***Figure 1-Figure supplement 2***), which may, however, be partly due to the small number of density samples (N=12 in both cases). Thus, the mouse and baboon data—with large samples sizes (N=42 and N=142, respectively)—suggest that it is the neuron densities that follow a lognormal distribution but not necessarily the glia densities.

Finally, we perform a control test on the different staining types—Nissl and NeuN—using the macaque$_1$ data. The staining methods differ in their treatment of glia: NeuN tends to label neuronal cell bodies only while Nissl indiscriminately labels both neurons and glia (***Yurt et al., 2018***). We show that regardless of staining type the cell densities pass the lognormality test (***Figure 1-Figure supplement 3***; SW test on $\ln(\rho)$ with $p > 0.05$), suggesting that counting some glia in the cell densities does not confound our analysis of the macaque$_1$ data.

Taken together, the normality test, the quantile plots, the pairwise tests, the cell type comparison, and the staining method comparison provide compelling evidence that the logarithmized neuron densities are normally distributed across cytoarchitectonic areas. This also holds for uniformly

sampled neuron densities (baboon) but not for a sampling that is neither uniform nor based on a cytoarchitectonic parcellation (macaque$_2$, galago$_2$). Thus, the neuron densities are consistent with a lognormal distribution across the different cortical areas, as long as sampling is not irregular.

Lognormal distribution of neurons within marmoset cortical areas

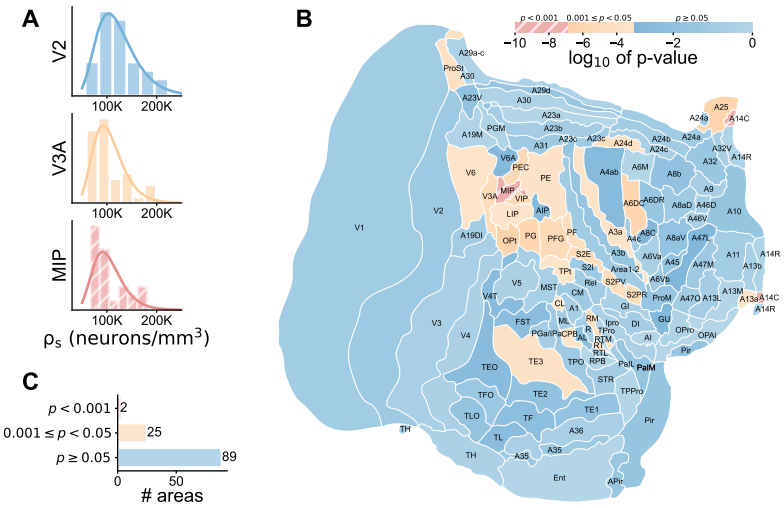

Figure 2. Neuron densities ρ_s follow a lognormal distribution within most areas of marmoset cortex. A Sample histograms of ρ_s and fitted lognormal distributions for three areas representing different degrees of lognormality. **B** Log_{10} of p-value of Shapiro-Wilk normality test of $\ln(\rho_s)$ on a flattened representation of the marmoset cortex (***Atapour et al., 2019***). **C** Number of areas with p-values in the given significance ranges.

To investigate whether the lognormal distribution holds within cortical areas, we leverage detailed estimates of neuron density in marmoset (***Atapour et al., 2019***). Neurons were counted within $150 \times 150\ \mu m$ counting frames for four strips per cortical area, all originating from the same subject. The within-area distributions of the sampled neuron densities ρ_s across the counting frames in three representative areas (MIP, V2, and V3; ***Figure 2***A) again suggest a lognormal distribution. As before, we check for lognormality by testing $\ln(\rho_s)$ for normality with the SW-test (for full test results see ***Table S2***). At significance level $\alpha = 0.05$, the normality hypothesis is not rejected for 89 out of 116 areas; whereas at $\alpha = 0.001$, this is the case for 114 out of 116 areas (***Figure 2***B,C). Thus, regardless of the precise significance threshold, the lognormality hypothesis cannot be rejected within most cortical areas in the marmoset cortex.

Statistical model comparison

To complement the statistical hypothesis tests on the logarithmic densities, we compared the lognormal model with six other statistical distributions based on the relative likelihood (see Statistical model comparison). We included statistical distributions with support in $\mathbb{R}^+$ since neuron densities cannot be negative: lognormal, truncated normal, inverse normal, gamma, inverse gamma, Lévy, and Weibull. Of these, the lognormal, inverse normal, and inverse gamma distributions stand out as the distributions with the highest relative likelihoods, both across the entire cortex and within cortical areas (***Figure 3***A, ***Figure 3-Figure supplement 1***A). A visual inspection of the fitted distributions reveals that the lognormal, inverse normal, and inverse gamma distributions produce virtually indistinguishable probability densities (***Figure 3***B, ***Figure 3-Figure supplement 1***C); indeed, the relative likelihoods of the three models are above 0.05 in all cases. This suggests that the data could theoretically be distributed according to either the lognormal, inverse normal, or inverse gamma distribution. To narrow down the model comparison, we show below how the lognormal

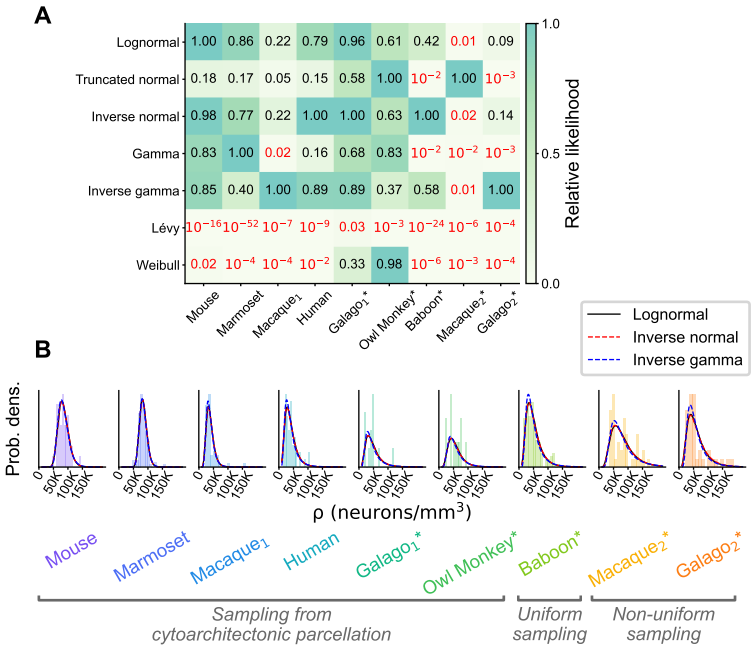

Figure 3. Statistical model comparison across the entire cortex of different animals. A Relative likelihood for seven compatible statistical models for all available area-level neuron density data sets; numerical values indicated for each model and animal. The red color indicates a relative likelihood < 0.05 with respect to the model with the highest likelihood. **B** The three best statistical models (according to the relative likelihood) fitted to the neuron density histograms in each animal; the three models produce visually nearly indistinguishable fits.

distribution could arise from the simple biophysical process of noisy cell division. In contrast, we are not aware of a simple mechanism that could give rise to inverse normal or inverse gamma distributions.

A minimal model for the emergence of lognormally distributed neuron densities

The finding of lognormally distributed neuron densities raises the question how the intricate process of neurogenesis (***Rakic, 2009***; ***Dehay and Kennedy, 2007***; ***Cadwell et al., 2019***) culminates in this distribution within and across areas in several mammalian species.

On the within-area level, a minimal model shows that there is no need for a specific regulatory mechanism (see Model of neurogenesis with variability for further details): assuming that the proliferation of the neural progenitor cells is governed by a noisy rate $\lambda_P(t) + \xi(t)$, where $\lambda_P(t)$ denotes the mean rate and $\xi(t)$ is a zero-mean Gaussian white noise, the resulting density of progenitor cells is lognormally distributed. The cells produced by the cell division of the neural progenitor cells are terminally differentiated neurons, which thus do not divide further. This renders the final neuron density a linear integral of the (changing) neural progenitor cell density. While this additive process formally does not preserve the lognormality of the neural progenitor density, the resulting neuron density distribution is closely approximated by a lognormal distribution with matched moments (***Figure 4***B and ***Figure 4-Figure supplement 1***F)—akin to the lognormal approximation for the sum of independent lognormal random variables (***Fenton, 1960***; ***Marlow, 1967***). Put differently, the lognormally distributed density of neural progenitor cells leads to an approximately lognormally distributed density of neurons. Thus, the lognormal neuron density distribution within areas could be a hallmark of a progenitor cell proliferation process with variability.

On the across-area level, the proliferation times for each area become relevant, since they vary up to twofold (***Rakic, 2002***). We therefore hypothesize that the distribution of proliferation times

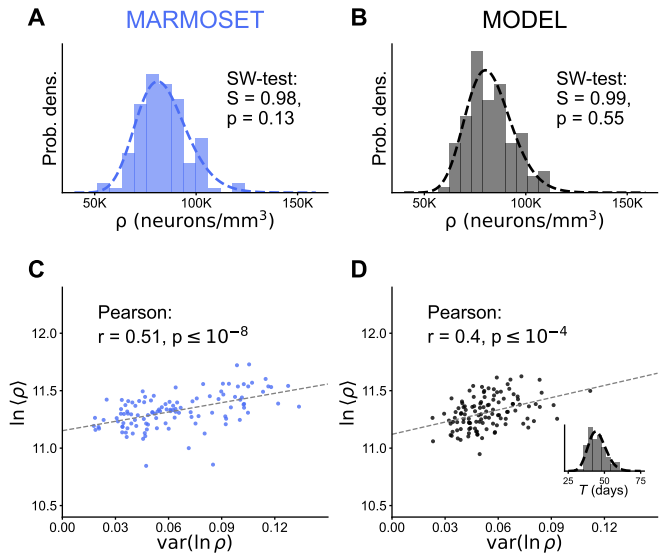

Figure 4. Neuron densities in the marmoset are compatible with a minimal model of neurogenesis with variability. A, B Distribution of neuron densities across areas for the marmoset (**A**) and the model (**B**). The Shapiro-Wilk test does not reject normality of $\ln(\rho)$ for both distributions. **C, D** The logarithmic mean $\ln(\langle\rho\rangle)$ and the variance of the logarithmic density $\mathrm{var}(\ln(\rho))$ for each area are significantly correlated with each other (Pearson correlation test) for the marmoset (**C**) and the model (**D**). The inset in **D** displays the inferred distribution (dashed line; see Equation (14)) of proliferation times alongside the sample used for the simulation (bars). For all parameters of the model and further details see Model of neurogenesis with variability.

is the most important source of the variability across areas (variability due to area-specific proliferation rates (***Lukaszewicz et al., 2005***) is discussed below). Since the average neuron density within an area is determined by the proliferation time, the distribution of proliferation times specifies the distribution of area-averaged neuron densities across areas. This relation can be inverted to determine the distribution of proliferation times from the lognormal distribution of (within-area) average neuron densities (see Model of neurogenesis with variability). A specific prediction of this model is that the logarithmic mean $\ln(\langle\rho\rangle)$ and variance of $\ln(\rho)$ are related through the proliferation time—both mean and variability increase with proliferation time in approximate proportion to each other (see Equations (11) and (13), respectively). Indeed, we observe a linear correlation in the marmoset data (Pearson $r = 0.51,\ p \leq 10^{-8}$, ***Figure 4***C) as well as in the data produced by the model (Pearson $r = 0.4,\ p \leq 10^{-4}$, ***Figure 4***D).

Discussion

In this work we show that neuron densities are compatible with a lognormal distribution across cortical areas in multiple mammalian cortices and within most cortical areas of the marmoset, uncovering a ubiquitous organizational principle of cerebral cortex. The distributions of neuron and cell densities in general depend on the underlying spatial sampling: We found that neuron densities follow a lognormal distribution within cytoarchitectonically defined areas, across such areas, and when averaged within small parcels uniformly sampled across cortex, but not when sampled in a highly non-uniform manner not following cytoarchitectonic boundaries.

Furthermore, we show that none of a sizeable list of statistical models outperform the lognormal distribution. Our results are in agreement with the observation that surprisingly many characteristics of the brain follow lognormal distributions (***Buzsáki and Mizuseki, 2014***). Moreover, this analysis highlights the importance of characterizing the statistical distributions of brain data because simple summary statistics—such as the mean or standard deviation—lack nuance and are

not necessarily a good representation of the underlying data.

Finally, we propose a minimal model that accounts for the emerging lognormal distributions based on a noisy cell division process of the neural progenitor cells and their specification to neurons. In principle, a multiplicative process with Gaussian noise leads to lognormal distributions at any scale; the additive specification from progenitors to neurons approximately preserves the lognormality. However, this noisy process alone cannot explain the coexistence of lognormal distributions of ρ at different scales (within and across areas). When the distributed proliferation times are considered, the model can account for both within-area and across-area distributions.

The model explains the observed lognormality based on a minimal set of assumptions; hence, we did not include further mechanisms like cell death (apoptosis), migration, volumetric growth, the generation of other postmitotic cells, or area-specific proliferation rates. However, none of these additional mechanisms affect the main conclusions. Apoptosis is a widespread phenomenon (***Oppenheim, 1991***; ***Inglis-Broadgate et al., 2005***; ***Kalinichenko and Matveeva, 2008***) during neurogenesis and it can be modeled as a multiplicative process affecting the neuron density alone. Thus, the neuron density still depends linearly on the progenitor cell density and approximately maintains lognormality. While apoptosis could add to the inter-area variability, our model shows that it is not necessary for the distribution of variability per se—in agreement with ***Oppenheim et al. (1989***) who found that the final pattern of spatial variability in spinal motoneuron density was already present before the onset of cell death and migration. Following the radial unit hypothesis (***Rakic, 2009***) we focus on radial migration of progenitor cells, ignoring tangential migration. In our model this assumption can be relaxed as long as there is no net increase or decrease in progenitor cell density due to tangential migration. Furthermore, we modeled the cell density in a fixed final target volume; thus, the effects of volumetric growth do not affect the model. The generation of other postmitotic cell types would reduce the effective proliferation rate of progenitor cells; this only leads to quantitative but not qualitative changes in the resulting distributions. Finally, it has been shown that cortical areas can have different proliferation rates (***Polleux et al., 1997***; ***Lukaszewicz et al., 2005***; ***Dehay and Kennedy, 2007***). If the proliferation rates are constant in time and lognormally distributed across areas, this additional variability would broaden the neuron density distribution but preserve the lognormal shape. However, in contrast to distributed proliferation times, it would not lead to the correlation between mean density and variability seen in the data (***Figure 4***C), because the proliferation rate affects the mean density but not the variance of the logarithmic progenitor density (see Eq. (7)). Furthermore, to the best of our knowledge, a difference in proliferation rate has only been shown for areas V1 and V2 (***Lukaszewicz et al., 2005***; ***Dehay and Kennedy, 2007***)—thus, we speculate that this is an important reason for the drastically higher neuron density in V1.

In principle, cortex-wide organizational structures might be by-products of development or evolution that serve no computational function (***Otopalik et al., 2017***)—but the fact that we observe the same organizational principle for several species and across most cortical areas suggests that the lognormal distribution serves some purpose. Heterogeneous neuron densities could assist computation through their association with heterogeneity in other properties such as connectivity and neuronal time constants (***Hilgetag et al., 2019***; ***Rall, 1969***); indeed, such heterogeneity is known to be a valuable asset for neural computation (***Duarte and Morrison, 2019***; ***Perez-Nieves et al., 2021***). Alternatively, localized concentration of neurons in certain areas and regions could also serve a metabolic purpose since centralization might support efficient transport of metabolites across neurons and astrocytes (***Bélanger et al., 2011***; ***Magistretti and Allaman, 2015***). Energy efficiency is particularly relevant since a large portion of the brain's energy consumption is used to support the communication between neurons (***Attwell and Laughlin, 2001***; ***Laughlin and Sejnowski, 2003***). Also from the perspective of cortical hierarchies it makes sense to have few areas with high neuron densities and many areas with lower neuron densities: Low-density areas contain neurons with large dendritic trees (***Elston and Rosa, 1998***) receiving convergent inputs from many neurons in high-density areas lower in the hierarchy. The neurons with extensive dendritic

trees in higher areas are involved in different, area-specific abstractions of the low-level sensory information (***Kumar et al., 2007***; ***Brincat et al., 2018***). All in all, there is probably not a single factor that leads to lognormal neuron densities in the cortex; further research will be needed to refine our findings and uncover the functional implications.

Materials and methods

Cell density data

Estimates of neuron density for the available cortical areas across the mouse (*Mus musculus*), marmoset (*Callithrix jacchus*), macaque (*Macaca mulatta*), human (*Homo sapiens*), galago (*Otolemur garnettii*), owl monkey (*Aotus nancymaae*), and baboon (*Papio cynocephalus anubis*) cerebral cortex were used in this study.

In the cases of mouse, marmoset, macaque$_1$, human, galago$_1$, and owl monkey the data were sampled from standard cytoarchitectonic parcellations; abbreviated names for all areas are listed in ***Table S1***. Note that we use subscript indices to distinguish between different data sets on the same model animal, e.g., macaque$_1$ and macaque$_2$.

Neuron density estimates for the mouse were published by ***Erö et al.*** (***2018***), and were measured from previously published Nissl-body-stained slices (***Lein et al., 2007***), where genetic markers were used to distinguish between cell types. The data were provided in the Allen Brain Atlas parcellation (***Lein et al., 2007***; ***Dong, 2008***). To estimate the quantitative neuron and cell densities ***Erö et al.*** (***2018***) used "a variety of whole brain image datasets [from the Allen Mouse Brain Atlas]"; as well as "some values reported from anatomical experiments in the literature", such as from (***Herculano-Houzel et al., 2013***).

Neuron density estimates for the marmoset cortex were published by ***Atapour et al.*** (***2019***), and were measured from NeuN-stained slices. The data were provided in the Paxinos parcellation (***Paxinos et al., 2011***) and all quantitative values are derived from the same brain of a single subject. Neuron densities within each counting frame used in the original publication (***Atapour et al., 2019***, Figure S1) were obtained via personal communication with Nafiseh Atapour, Piotr Majka, and Marcello G. Rosa.

The neuron density estimates in the first macaque data set, macaque$_1$, were previously published in visual form by ***Beul and Hilgetag*** (***2019***), and were obtained from both Nissl-body- and NeuN-stained brain slices. Most of the numerical values were reported by ***Dombrowski et al.*** (***2001***) and ***Hilgetag et al.*** (***2016***), and the remaining values were provided by Sarah F. Beul and Claus C. Hilgetag via personal communication. Counts based on Nissl-body staining were scaled according to a linear relationship with the counts from NeuN staining obtained from selected areas where both types of data were available (***Beul and Hilgetag, 2019***). The data follow the M132 parcellation (***Markov et al., 2014***) and constitute the average across subjects.

Cell density estimates for the human cortex were previously published by ***von Economo et al.*** (***2008***), and were measured from Nissl-body-stained brain slices. The human data therefore most likely reflect combined neuron and glia densities. The data were provided in the von Economo parcellation (***von Economo et al., 2008***); all quantitative values are based on "the mean of the numbers gathered from the various brains" (***von Economo et al., 2008***, p. 201).

Cell and neuron density estimates for galago$_{1\&2}$, owl monkey, baboon, and macaque$_2$ were previously published by ***Collins et al.*** (***2010***), and were measured using the isotropic fractionator method. The data are sampled from common parcellation schemes in galago$_1$ and owl monkey, approximately equal-size samples in the baboon, and irregular non-uniform samples in macaque$_2$ and galago$_2$. All the quantitative values were derived from one hemisphere of each subject separately. Each data set thus describes only a single subject, without combining data across individuals of the same species.

Statistical model comparison

In order to assess which model is most compatible with the data, we compared the relative likelihood of different distributions against each other. We included an extensive list of distributions with support on $\mathbb{R}^+$, estimated the distributions' parameters using maximum likelihood, and calculated the Akaike Information Criterion (AIC)

$$AIC = 2k - 2\ln\mathcal{L} \tag{1}$$

where k is the number of estimated parameters of the model and $\mathcal{L}$ is the estimated maximum likelihood. We further compare the models using the relative likelihood ($\mathcal{L}_r$)

$$\mathcal{L}_r = e^{(AIC_{\min} - AIC_i)/2} \tag{2}$$

where $AIC_{\min}$ is the minimum AIC across all models and AIC_i is the AIC for the ith model. The relative likelihood indicates the probability that, from among the tested models, the ith model most strongly limits the information loss (***Burnham and Anderson, 2004***). We take a significance threshold of $\alpha = 0.05$ on the relative likelihood to determine whether a model is significantly worse than the best possible model.

Model of neurogenesis with variability

Within areas

Neurons are generated through symmetric or asymmetric cell division of neural progenitor cells (***Cadwell et al., 2019***). Grouping all types of progenitor cells into a single population P, all neurons into a population N, and excluding other post-mitotic cell types, their population size can be modeled by the coupled system of differential equations (***Picco et al., 2018***)

$$\frac{d}{dt}P = \lambda_P P - \lambda_N P, \qquad \frac{d}{dt}N = \lambda_N P, \tag{3}$$

where λ_P denotes the (potentially time-dependent) rate of progenitor generation and λ_N the (potentially time-dependent) rate of neuron generation.

Following the radial unit hypothesis (***Rakic, 2009***), we consider a small number of such radial units (small compared to the total size of the area) and determine the density of progenitors ρ_P and neurons ρ_N in these radial units by dividing through the volume V of the considered radial units in the fully developed cortex. Importantly, this reference volume is the same for every area. Since Equation (3) is linear, dividing by V leads to

$$\frac{d}{dt}\rho_P = \lambda_P \rho_P - \lambda_N \rho_P, \qquad \frac{d}{dt}\rho_N = \lambda_N \rho_P. \tag{4}$$

Note that this does not necessarily exclude tangential migration as long as the net influence of the tangential migration is zero.

Progenitor cell proliferation

First, we consider the proliferation of the progenitor cells, which we assume to be governed by a noisy rate. Modeling the noise by a zero-mean, unit-strength Gaussian white noise process ξ, we obtain a stochastic differential equation (SDE) for the progenitor cell density

$$\frac{d}{dt}\rho_P = (\lambda_P - \lambda_N + \sigma\xi)\rho_P \tag{5}$$

where σ controls the (potentially time-dependent) intensity of the noise. Using the Stratonovich interpretation—assuming that the noise process has a small but finite correlation time before taking the white-noise limit (***Van Kampen, 2007***)—the stochastic differential equation transforms by the same rules as an ordinary differential equation (***Van Kampen, 2007***) such that we can rewrite the SDE (5) as $\frac{d}{dt}\ln\rho_P = \lambda_P - \lambda_N + \sigma\xi$ with the solution

$$\ln\rho_P(t) = \ln\rho_0 + \int_0^t \big(\lambda_P(s) - \lambda_N(s)\big)ds + \int_0^t \sigma(s)\xi(s)ds. \tag{6}$$

Since $\xi(t)$ is Gaussian and Equation (6) is linear, $\ln\rho_P(t)$ is Gaussian and hence $\rho_P(t)$ is lognormally distributed at all times t. The parameters of this lognormal distribution are the mean of the logarithmic progenitor cell density $\mu_P(t) = \langle \ln\rho_P(t)\rangle$ and the variance of the logarithmic progenitor cell density $\sigma_P(t)^2 = \langle \Delta(\ln\rho_P(t))^2\rangle$ (here $\Delta x \equiv x - \langle x\rangle$). Using Equation (6), $\langle\xi(s)\rangle = 0$, and $\langle\xi(s)\xi(s')\rangle = \delta(s-s')$, we obtain (cf., for instance ***Braumann*** (***2007***))

$$\mu_P(t) = \ln\rho_0 + \int_0^t \big(\lambda_P(s) - \lambda_N(s)\big)ds \qquad \text{and} \qquad \sigma_P(t)^2 = \int_0^t \sigma(s)^2 ds. \tag{7}$$

Thus, the progenitor cell densities are lognormally distributed at all times with parameters $\mu_P(t)$ and $\sigma_P(t)^2$. The corresponding first two moments of the progenitor cell density are

$$\langle \rho_P(t) \rangle = \exp\left(\mu_P(t) + \frac{1}{2}\sigma_P(t)^2\right), \qquad \langle \rho_P(t)\rho_P(t') \rangle = \langle \rho_P(t) \rangle \langle \rho_P(t') \rangle \exp\left(\int_0^{\min(t,t')} \sigma(s)^2 ds\right), \tag{8}$$

where we used the characteristic functional of the Gaussian white noise $\xi(t)$ (***Van Kampen, 2007***), $\langle \exp(i \int_{-\infty}^{\infty} k(s)\sigma(s)\xi(s)ds) \rangle = \exp(-\frac{1}{2}\int_{-\infty}^{\infty} \sigma(s)^2 k(s)^2)$, with the test function $ik(s) = \mathbb{1}_{[0,t]}(s)$ for the first moment (here $\mathbb{1}_A(s)$ denotes the indicator function) and test function $ik(s) = \mathbb{1}_{[0,t]}(s) + \mathbb{1}_{[0,t']}(s)$ for the second moment as well as $\int_{-\infty}^{\infty} \mathbb{1}_{[0,t]}(s)\mathbb{1}_{[0,t']}(s)\sigma(s)^2 ds = \int_0^{\min(t,t')} \sigma(s)^2 ds$.

Neurogenesis

Next, we consider neurogenesis. We assume that the noise affects primarily the rate of progenitor cell proliferation. The solution to Equation (4) for a given $\rho_P(t)$ and initial condition $\rho_N(0) = 0$ is

$$\rho_N(t) = \int_0^t \lambda_N(s)\rho_P(s)ds. \tag{9}$$

Since $\rho_N(t)$ is the integral of the (temporally correlated) lognormal process $\rho_P(s)$ it is formally not lognormal. However, the sum of independent lognormal random variables is well approximated by a lognormal distribution with matched first and second moment (***Fenton, 1960***; ***Marlow, 1967***). Here, we extend this approximation to the integral of temporally correlated lognormal processes. The first two moments of the neuron density follow from the averages of Equation (9),

$$\langle \rho_N(t) \rangle = \int_0^t \lambda_N(s)\langle \rho_P(s) \rangle ds, \qquad \langle \rho_N(t)^2 \rangle = \int_0^t \int_0^t \lambda_N(s)\lambda_N(s')\langle \rho_P(s)\rho_P(s') \rangle ds ds'. \tag{10}$$

The lognormal approximation with matched moments is parameterized by

$$\mu_N(t) = \ln\langle \rho_N(t) \rangle - \frac{1}{2}\sigma_N(t)^2, \qquad \sigma_N(t)^2 = \ln\left(1 + \frac{\langle \Delta(\rho_N(t))^2 \rangle}{\langle \rho_N(t) \rangle^2}\right), \tag{11}$$

where we used $\langle x \rangle = \exp(\mu + \frac{1}{2}\sigma^2)$ and $\langle \Delta x^2 \rangle = \langle x \rangle^2[\exp(\sigma^2) - 1]$ for a lognormal variable x. Note that the parameters of the lognormal distribution are the mean of the logarithmic neuron density $\mu_N(t) = \langle \ln \rho_N(t) \rangle$ and the variance of the logarithmic neuron density $\sigma_N(t)^2 = \langle \Delta(\ln \rho_N(t))^2 \rangle$.

In the parameter regime determined by the experimental data, the lognormal approximation is statistically indistinguishable from the true distribution (SW test $p = 0.4$ for 2000 samples; ***Figure 4-Figure supplement 1***F).

Across areas

Thus far, the model accounts for the lognormal distribution of neuron densities within an area. Across areas, we hypothesize that the distribution of proliferation times (***Rakic, 2002***; ***Cadwell et al., 2019***) is the most important cause of the variability in the neuron densities. To characterize an individual area, we consider the average density $\langle \rho_N(t) \rangle$. For convenience, we introduce the auxiliary quantity

$$y(t) = \ln\left(\int_0^t \lambda_N(s) \exp\left(\int_0^s \left(\lambda_P(r) - \lambda_N(r)\right)dr + \frac{1}{2}\int_0^s \sigma(r)^2 dr\right)ds\right) \tag{12}$$

such that the logarithm of the mean neuron density simplifies to

$$\ln\langle \rho_N(t) \rangle = \ln \rho_0 + y(t) \tag{13}$$

where we inserted Equation (7) into Equation (8) to obtain the mean of the progenitor cell density, which we then plugged into Equation (10).

In order to arrive at a lognormal distribution of the mean density $\langle \rho_N(t) \rangle$ across areas, the terms on the r.h.s. of Equation (13) have to be normally distributed. In particular, this means that the proliferation times have to be distributed such that $y(t)$ is Gaussian. The distribution $p(y)$ of $y = y(t)$,

which is a strictly monotonic transformation of the proliferation time t, is related to the distribution of proliferation times $p(t)$ through (***Van Kampen, 2007***)

$$p(t) = \left|\frac{dy}{dt}\right| \mathcal{N}\left(y(t) \mid \mu_y, \sigma_y^2\right). \tag{14}$$

The first factor on the r.h.s. can be obtained from Equation (12) and the second factor is a Gaussian probability density with mean μ_y and variance σ_y^2. Hence, Equation (14) fully specifies the distribution of proliferation times; conversely, for proliferation times distributed according to Equation (14), the mean neuron density $\langle \rho_N(t) \rangle$ is lognormally distributed across areas. Note that since the Gaussian has support on the entire real line, the neuron density needs to diverge for $t \to \infty$. Thus, we restrict $\lambda_P(t)$, $\lambda_N(t)$, and $\sigma(t)$ such that the neuron density would diverge in the hypothetical limit of an infinite proliferation time.

Parameter estimation

Above, we showed how a noisy rate of progenitor proliferation leads to a lognormal distribution of progenitor cell densities and neuron densities within an area and, for the distribution of proliferation times (14), to a lognormal distribution of (within-area) mean neuron densities across areas. In order to compare the predictions of the model with the data, we estimate the model's parameters using the available experimental data.

We restrict the analysis to the simplified case of constant rate λ_P, λ_N, and noise intensity σ and identical rates of progenitor and neuron proliferation, $\lambda_P = \lambda_N \equiv \lambda$. In particular the assumption of a constant rate (note that this is not a necessary assumption for the above theory) is simplifying because the cell cycle length varies during development (***Kornack and Rakic, 1998***). Despite this simplifying assumption, the model quantitatively matches the data for the parameters inferred below (***Figure 4***).

First, we determine the rate λ from the average cell cycle length of progenitor cells determined from a short period of 2 hours (***Kornack and Rakic, 1998***) such that fluctuations and the conversion of progenitor cells to neurons can be neglected. For a given cell cycle length ℓ, the number of cells increases as $2^{t/\ell} = \exp\left(t \ln(2)/\ell\right)$. Thus, the cell cycle length ℓ corresponds to a proliferation rate $\lambda = \ln(2)/\ell$. Using the average cell cycle length of $\ell \approx 1.5\,\text{days}$ from macaque (***Kornack and Rakic, 1998***; ***Picco et al., 2018***), we obtain $\lambda \approx 0.46\,\text{days}^{-1}$. The proliferation time of areas varies between 30 and 60 days in macaque (***Rakic, 2002***) which we expect to be similar in the marmoset since macaques and marmosets have similar gestation times of 5.5 and 4.5 months, respectively (***Schultz-Darken et al., 2016***). Thus, we set the median proliferation time per area to $t_{1/2} = 45$ days, which determines $\mu_y = y(t_{1/2})$ because the median of the distribution (14) is given by $\frac{1}{2} = \int_0^{t_{1/2}} p(t)dt = \int_{-\infty}^{y(t_{1/2})} \mathcal{N}(y \mid \mu_y, \sigma_y^2)dy$ and the median of the normal distribution is at $y = \mu_y$.

In addition, the mean μ_y of the auxiliary variable y is also constrained by the distribution of the variance σ_N^2 of the logarithmic neuron density across areas; we will use this additional constraint to determine the noise intensity σ. For a fixed proliferation time t, $\sigma_N(t)^2$ is given by Equation (11). Since σ_N^2 is a strictly monotonically increasing function of t, its distribution can be written in terms of that of the inverse $t(\sigma_N^2)$, i.e., $p(\sigma_N^2) = \left|\frac{dt}{d\sigma_N^2}\right| p\left(t(\sigma_N^2)\right)$. Using Equation (14) for the distribution of proliferation times $p(t)$ and Equation (12) to relate $y(t)$ and t, the distribution of σ_N^2 across areas is thus

$$p(\sigma_N^2) = \frac{1}{|f'(f^{-1}(\sigma_N^2))|} \mathcal{N}\left(f^{-1}(\sigma_N^2) \mid \mu_y, \sigma_y^2\right) \tag{15}$$

where $f(y) = \sigma_N^2(t(y))$ with $t(y)$ the inverse of

$$y(t) = \ln \frac{2\lambda}{\sigma^2} + \ln(e^{\frac{1}{2}\sigma^2 t} - 1), \tag{16}$$

which follows from evaluating Equation (12) with $\lambda_P = \lambda_N \equiv \lambda$ and constant σ^2, and $f^{-1}(\sigma_N^2)$ is the inverse of $f(y)$. Explicitly, it is given by

$$f^{-1}(\sigma_N^2) = \ln \frac{\lambda}{\sigma^2} + \ln\left(\sqrt{8\left(3e^{\sigma_N^2} - 1\right)} - 4\right), \tag{17}$$

which follows from inserting $t(y)$ into $\sigma_N^2(t)$ determined by Equation (11) and solving it for y. The maximum likelihood estimator $\hat{\mu}_y$ for μ_y with the likelihood $p(\sigma_N^2)$ is the empirical average of $f^{-1}(\sigma_N^2)$ across areas because the Jacobian $1/|f'(f^{-1}(\sigma_N^2))|$ in Equation (15) does not depend on the parameters and hence does not affect the Gaussian likelihood of μ_y. Using the marmoset data, we obtain $\hat{\mu}_y \approx 3.07$. We finally arrive at $\sigma \approx 0.061\,\mathrm{days}^{-1/2}$ by enforcing $\hat{\mu}_y = y(t_{1/2})$, where $y(t)$ is given by Equation (16), with $t_{1/2} = 45$ days. With σ and μ_y determined, we choose σ_y such that less than 2% of the proliferation times are smaller than 30 days or larger than 60 days. This leads to $\sigma_y^2 \approx 0.02$.

It remains to estimate the initial progenitor density ρ_0. To this end, we consider the distribution of $\ln\langle\rho_N\rangle$. For a fixed proliferation time t, $\ln\langle\rho_N(t)\rangle$ is determined by Equation (13). Thus, it is also a monotonic transformation of the random variable t, with distribution $p(\ln\langle\rho_N\rangle) = \left|\frac{dt}{d\ln\langle\rho_N\rangle}\right| p\big(t(\ln\langle\rho_N\rangle)\big)$. Using the linear dependence between $\ln\langle\rho_N\rangle$ and y, Equation (13), in combination with the distribution of proliferation times (14), we obtain

$$p(\ln\langle\rho_N\rangle) = \mathcal{N}\big(\ln\langle\rho_N\rangle \mid \ln\rho_0 + \mu_y, \sigma_y^2\big). \tag{18}$$

The maximum likelihood estimator for $\ln\rho_0 + \mu_y$ is the empirical average of $\ln\langle\rho_N\rangle$ across areas; subtracting μ_y we obtain $\rho_0 \approx 3.8 \times 10^3$ cells/mm^3.

Note that in the simplified case considered here, the resulting distribution of proliferation times approaches a lognormal distribution in the left tail and a Gaussian in the right tail: for small times, $\frac{1}{2}\sigma^2 t \ll 1$, a Taylor expansion of $y(t)$ leads to $y(t) \approx \ln(\lambda t)$ and thus a lognormal distribution; for large times, $\frac{1}{2}\sigma^2 t \gg 1$, $y(t)$ grows linearly with $y(t) \approx \ln\frac{2\lambda}{\sigma^2} + \frac{1}{2}\sigma^2 t$ and thus the distribution approaches a Gaussian.

Simulation Details

We solve the SDE (5) using the Euler-Maruyama method with time step $\Delta t = 0.05$ in total N_{sample} times with identical parameters for each of the 114 areas. Because the number of samples per area N_{sample} varies, we randomly choose N_{sample} for each area following $N_{\mathrm{sample}} \sim \mathrm{Poisson}(36.6)$ where 36.6 is the average sample size per cortical area in the marmoset data. The subsequent analysis of the model data is identical to the analysis of the experimental data.

Acknowledgements

This work was supported by the European Union Horizon 2020 Framework Programme for Research and Innovation (Human Brain Project SGA2 grant number 785907 and HBP SGA3 grant number 945539) and the Deutsche Forschungsgemeinschaft (DFG, German Research Foundation) under Priority Program (SPP 2041 "Computational Connectomics") [S.J. van Albada: AL 2041/1-1 and 2041/1-2] and Open Access Publication Costs grant 491111487.

We thank Günther Palm for helpful discussions, Alexandre René for helpful discussions and support with the Bayesian model comparison, Anno Kurth for discussions about geometric Brownian motion, and Jon Martinez Corral for proofreading an early draft.

Author contributions: Conceptualization AMG, AvM, SvA; Data curation AMG; Formal Analysis AMG, AvM; Funding acquisition SvA; Investigation AMG, AvM, SvA; Methodology AMG, AvM, SvA; Project administration SvA; Resources SvA; Software AMG, AvM; Supervision SvA; Validation AvM; Visualization AMG; Writing - original draft AMG, AvM; Writing – review & editing AMG, AvM, SvA.

Competing interests: The authors declare no competing interests.

Data and materials availability: This work produced no new data and instead relied on a corpus of neuron density data available from the literature, which we gratefully acknowledge; see Cell density data for a detailed description.

References

van Albada SJ, Morales-Gregorio A, Dickscheid T, Goulas A, Bakker R, Bludau S, Palm G, Hilgetag CC, Diesmann M. Bringing Anatomical Information into Neuronal Network Models. In: Giugliano M, Negrello M, Linaro D, editors. *Computational Modelling of the Brain: Modelling Approaches to Cells, Circuits and Networks* Cham: Springer International Publishing; 2022.p. 201–234. doi: 10.1007/978-3-030-89439-9_9.

Atapour N, Majka P, Wolkowicz IH, Malamanova D, Worthy KH, Rosa MGP. Neuronal Distribution Across the Cerebral Cortex of the Marmoset Monkey (Callithrix jacchus). Cerebral cortex. 2019; 29(9):3836–3863. doi: 10.1093/cercor/bhy263.

Attwell D, Laughlin SB. An Energy Budget for Signaling in the Grey Matter of the Brain. Journal of Cerebral Blood Flow & Metabolism. 2001 Oct; 21(10):1133–1145. http://journals.sagepub.com/doi/10.1097/00004647-200110000-00001, doi: 10.1097/00004647-200110000-00001.

von Bartheld CS, Bahney J, Herculano-Houzel S. The search for true numbers of neurons and glial cells in the human brain: A review of 150 years of cell counting: Quantifying neurons and glia in human brain. Journal of Comparative Neurology. 2016 Dec; 524(18):3865–3895. https://onlinelibrary.wiley.com/doi/10.1002/cne.24040, doi: 10.1002/cne.24040.

Beul SF, Hilgetag CC. Neuron density fundamentally relates to architecture and connectivity of the primate cerebral cortex. NeuroImage. 2019; 189:777–792. https://www.sciencedirect.com/science/article/pii/S1053811919300102, doi: 10.1016/j.neuroimage.2019.01.010.

Braitenberg V, Schüz A. Anatomy of the Cortex: Statistics and Geometry. Berlin, Heidelberg, New York: Springer-Verlag; 1991.

Braumann CA. Itô versus Stratonovich calculus in random population growth. Mathematical Biosciences. 2007; 206(1):81–107.

Brincat SL, Siegel M, von Nicolai C, Miller EK. Gradual progression from sensory to task-related processing in cerebral cortex. Proceedings of the National Academy of Sciences. 2018 Jul; 115(30). https://doi.org/10.1073/pnas.1717075115, doi: 10.1073/pnas.1717075115.

Brodmann K. Vergleichende Lokalisationslehre der Großhirnrinde in ihren Prinzipien dargestellt auf Grund des Zellenbaues. Leipzig: Johann Ambrosius Barth; 1909.

Burnham KP, Anderson DR, editors. Model Selection and Multimodel Inference. Springer New York; 2004. https://doi.org/10.1007/b97636, doi: 10.1007/b97636.

Buzsáki G, Mizuseki K. The log-dynamic brain: how skewed distributions affect network operations. Nature Reviews Neuroscience. 2014; 15(4):264–278. doi: 10.1038/nrn3687.

Bélanger M, Allaman I, Magistretti P. Brain Energy Metabolism: Focus on Astrocyte-Neuron Metabolic Cooperation. Cell Metabolism. 2011; 14(6):724–738. https://linkinghub.elsevier.com/retrieve/pii/S1550413111004207, doi: 10.1016/j.cmet.2011.08.016.

Cadwell CR, Bhaduri A, Mostajo-Radji MA, Keefe MG, Nowakowski TJ. Development and Arealization of the Cerebral Cortex. Neuron. 2019; 103(6):980–1004.

Charvet CJ, Cahalane DJ, Finlay BL. Systematic, Cross-Cortex Variation in Neuron Numbers in Rodents and Primates. Cerebral Cortex. 2015; 25(1):147–160. https://academic.oup.com/cercor/article-lookup/doi/10.1093/cercor/bht214, doi: 10.1093/cercor/bht214.

Collins CE, Airey DC, Young NA, Leitch DB, Kaas JH. Neuron densities vary across and within cortical areas in primates. Proceedings of the National Academy of Sciences. 2010; 107(36):15927–15932. doi: 10.1073/pnas.1010356107.

Collins CE, Turner EC, Sawyer EK, Reed JL, Young NA, Flaherty DK, Kaas JH. Cortical cell and neuron density estimates in one chimpanzee hemisphere. Proceedings of the National Academy of Sciences. 2016; 113(3):740–745. http://www.pnas.org/lookup/doi/10.1073/pnas.1524208113, doi: 10.1073/pnas.1524208113.

Dehay C, Kennedy H. Cell-cycle control and cortical development. Nature Reviews Neuroscience. 2007 Jun; 8(6):438–450. http://www.nature.com/articles/nrn2097, doi: 10.1038/nrn2097.

Dombrowski SM, Hilgetag CC, Barbas H. Quantitative Architecture Distinguishes Prefrontal Cortical Systems in the Rhesus Monkey. Cerebral Cortex. 2001; 11(10):975–988. https://academic.oup.com/cercor/article-lookup/doi/10.1093/cercor/11.10.975, doi: 10.1093/cercor/11.10.975, iSBN: 1047-3211 (Print)\r1047-3211 (Linking).

Dong HW. The Allen reference atlas: A digital color brain atlas of the C57Bl/6J male mouse. John Wiley & Sons inc.; 2008.

Dorkenwald S, Turner NL, Macrina T, Lee K, Lu R, Wu J, Bodor AL, Bleckert AA, Brittain D, Kemnitz N, Silversmith WM, Ih D, Zung J, Zlateski A, Tartavull I, Yu SC, Popovych S, Wong W, Castro M, Jordan CS, et al. Binary and analog variation of synapses between cortical pyramidal neurons. eLife. 2022 Nov; 11:e76120. https://elifesciences.org/articles/76120, doi: 10.7554/eLife.76120.

Duarte R, Morrison A. Leveraging heterogeneity for neural computation with fading memory in layer 2/3 cortical microcircuits. PLOS Computational Biology. 2019; 15(4):e1006781. https://dx.plos.org/10.1371/journal.pcbi.1006781, doi: 10.1371/journal.pcbi.1006781.

von Economo C, Koskinas GN, Triarhou LC. Atlas of Cytoarchitectonics of the Adult Human Cerebral Cortex. Karger; 2008.

Elston GN, Rosa M. Morphological variation of layer III pyramidal neurones in the occipitotemporal pathway of the macaque monkey visual cortex. Cerebral Cortex. 1998; 8(3):278–294.

Ercsey-Ravasz M, Markov NT, Lamy C, Van Essen DC, Knoblauch K, Toroczkai Z, Kennedy H. A Predictive Network Model of Cerebral Cortical Connectivity Based on a Distance Rule. Neuron. 2013; 80(1):184–197. doi: 10.1016/j.neuron.2013.07.036.

Erö C, Gewaltig MO, Keller D, Markram H. A Cell Atlas for the Mouse Brain. Frontiers in Neuroinformatics. 2018; 12:84. https://www.frontiersin.org/article/10.3389/fninf.2018.00084/full, doi: 10.3389/fninf.2018.00084.

Fenton LF. The Sum of Log-Normal Probability Distributions in Scatter Transmission Systems. IRE Transactions on communications systems. 1960; 8(1):57–67.

Gămănuţ R, Kennedy H, Toroczkai Z, Ercsey-Ravasz M, Van Essen DC, Knoblauch K, Burkhalter A. The mouse cortical connectome, characterized by an ultra-dense cortical graph, maintains specificity by distinct connectivity profiles. Neuron. 2018; 97(3):698–715.

Herculano-Houzel S, Watson C, Paxinos G. Distribution of neurons in functional areas of the mouse cerebral cortex reveals quantitatively different cortical zones. Frontiers in Neuroanatomy. 2013; 7. http://journal.frontiersin.org/article/10.3389/fnana.2013.00035/abstract, doi: 10.3389/fnana.2013.00035.

Hilgetag CC, Beul SF, van Albada SJ, Goulas A. An Architectonic Type Principle Integrates Macroscopic Cortico-Cortical Connections with Intrinsic Cortical Circuits of the Primate Brain. Network Neuroscience. 2019; 3(4):905–923.

Hilgetag CC, Medalla M, Beul SF, Barbas H. The primate connectome in context: Principles of connections of the cortical visual system. NeuroImage. 2016; 134:685–702. http://dx.doi.org/10.1016/j.neuroimage.2016.04.017, doi: 10.1016/j.neuroimage.2016.04.017.

Inglis-Broadgate SL, Thomson RE, Pellicano F, Tartaglia MA, Pontikis CC, Cooper JD, Iwata T. FGFR3 regulates brain size by controlling progenitor cell proliferation and apoptosis during embryonic development. Developmental Biology. 2005; 279(1):73–85.

Jardim-Messeder D, Lambert K, Noctor S, Pestana FM, de Castro Leal ME, Bertelsen MF, Alagaili AN, Mohammad OB, Manger PR, Herculano-Houzel S. Dogs Have the Most Neurons, Though Not the Largest Brain: Trade-Off between Body Mass and Number of Neurons in the Cerebral Cortex of Large Carnivoran Species. Frontiers in Neuroanatomy. 2017 Dec; 11:118. http://journal.frontiersin.org/article/10.3389/fnana.2017.00118/full, doi: 10.3389/fnana.2017.00118.

Kalinichenko SG, Matveeva NY. Morphological characteristics of apoptosis and its significance in neurogenesis. Neuroscience and Behavioral Physiology. 2008; 38(4):333–344. http://link.springer.com/10.1007/s11055-008-0046-7, doi: 10.1007/s11055-008-0046-7.

Kornack DR, Rakic P. Changes in cell-cycle kinetics during the development and evolution of primate neocortex. Proceedings of the National Academy of Sciences. 1998; 95(3):1242–1246. https://www.pnas.org/doi/abs/10.1073/pnas.95.3.1242, doi: 10.1073/pnas.95.3.1242.

Kumar S, Stephan KE, Warren JD, Friston KJ, Griffiths TD. Hierarchical Processing of Auditory Objects in Humans. PLoS Computational Biology. 2007 Jun; 3(6):e100. https://doi.org/10.1371/journal.pcbi.0030100, doi: 10.1371/journal.pcbi.0030100.

Laughlin SB, Sejnowski TJ. Communication in neuronal networks. Science. 2003 September; 301:1870–1874.

Lein ES, Hawrylycz MJ, Ao N, Ayres M, Bensinger A, Bernard A, Boe AF, Boguski MS, Brockway KS, Byrnes EJ, Chen L, Chen L, Chen TM, Chi Chin M, Chong J, Crook BE, Czaplinska A, Dang CN, Datta S, Dee NR, et al. Genome-wide atlas of gene expression in the adult mouse brain. Nature. 2007; 445(7124):168–176. http://www.nature.com/articles/nature05453, doi: 10.1038/nature05453.

Liewald D, Miller R, Logothetis N, Wagner HJ, Schüz A. Distribution of axon diameters in cortical white matter: an electron-microscopic study on three human brains and a macaque. Biological Cybernetics. 2014 Oct; 108(5):541–557. https://doi.org/10.1007/s00422-014-0626-2, doi: 10.1007/s00422-014-0626-2.

Loewenstein Y, Kuras A, Rumpel S. Multiplicative Dynamics Underlie the Emergence of the Log-Normal Distribution of Spine Sizes in the Neocortex In Vivo. Journal of Neuroscience. 2011; 31(26):9481–9488. https://www.jneurosci.org/content/31/26/9481, doi: 10.1523/JNEUROSCI.6130-10.2011.

Lukaszewicz A, Savatier P, Cortay V, Giroud P, Huissoud C, Berland M, Kennedy H, Dehay C. G1 phase regulation, area-specific cell cycle control, and cytoarchitectonics in the primate cortex. Neuron. 2005; 47(3):353–364.

Magistretti P, Allaman I. A Cellular Perspective on Brain Energy Metabolism and Functional Imaging. Neuron. 2015 May; 86(4):883–901. https://linkinghub.elsevier.com/retrieve/pii/S0896627315002597, doi: 10.1016/j.neuron.2015.03.035.

Markov NT, Ercsey-Ravasz M, Ribeiro Gomes AR, Lamy C, Magrou L, Vezoli J, Misery P, Falchier A, Quilodran R, Gariel MA, Sallet J, Gamanut R, Huissoud C, Clavagnier S, Giroud P, Sappey-Marinier D, Barone P, Dehay C, Toroczkai Z, Knoblauch K, et al. A weighted and directed interareal connectivity matrix for macaque cerebral cortex. Cerebral Cortex. 2014; 24(1):17–36. doi: 10.1093/cercor/bhs270.

Marlow N. A Normal Limit Theorem for Power Sums of Independent Random Variables. The Bell System Technical Journal. 1967; 46(9):2081–2089.

Oppenheim RW. Cell Death During Development of the Nervous System. Annual Review of Neuroscience. 1991 Mar; 14(1):453–501. https://www.annualreviews.org/doi/10.1146/annurev.ne.14.030191.002321, doi: 10.1146/annurev.ne.14.030191.002321.

Oppenheim RW, Cole T, Prevette D. Early regional variations in motoneuron numbers arise by differential proliferation in the chick embryo spinal cord. Developmental Biology. 1989 Jun; 133(2):468–474. https://linkinghub.elsevier.com/retrieve/pii/001216068990050X, doi: 10.1016/0012-1606(89)90050-X.

Otopalik AG, Sutton AC, Banghart M, Marder E. When complex neuronal structures may not matter. eLife. 2017; 6:e23508. https://elifesciences.org/articles/23508, doi: 10.7554/eLife.23508.

Paxinos G, Watson CRR, Petrides M, Rosa MG, Tokuno H. The Marmoset Brain in Stereotaxic Coordinates. Elsevier Science; 2011.

Perez-Nieves N, Leung VCH, Dragotti PL, Goodman DFM. Neural heterogeneity promotes robust learning. Nature Communications. 2021; 12(1):5791. https://www.nature.com/articles/s41467-021-26022-3, doi: 10.1038/s41467-021-26022-3.

Picco N, García-Moreno F, Maini PK, Woolley TE, Molnár Z. Mathematical Modeling of Cortical Neurogenesis Reveals that the Founder Population does not Necessarily Scale with Neurogenic Output. Cerebral Cortex. 2018; 28(7):2540–2550. doi: 10.1093/cercor/bhy068.

Polleux F, Dehay C, Moraillon B, Kennedy H. Regulation of Neuroblast Cell-Cycle Kinetics Plays a Crucial Role in the Generation of Unique Features of Neocortical Areas. The Journal of Neuroscience. 1997 Oct; 17(20):7763–7783. https://www.jneurosci.org/lookup/doi/10.1523/JNEUROSCI.17-20-07763.1997, doi: 10.1523/JNEUROSCI.17-20-07763.1997.

Rakic P. Neurogenesis in adult primate neocortex: an evaluation of the evidence. Nature Reviews Neuroscience. 2002; 3(1):65–71.

Rakic P. Evolution of the neocortex: a perspective from developmental biology. Nature Reviews Neuroscience. 2009 Oct; 10(10):724–735. doi: 10.1038/nrn2719.

Rall W. Time constants and electrotonic length of membrane cylinders and neurons. Biophysical Journal. 1969; 9(12):1483–1508.

Razali NM, Yap BW. Power Comparisons of Shapiro-Wilk, Kolmogorov-Smirnov, Lilliefors and Anderson-Darling Tests. Journal of Statistical Modeling and Analytics. 2011; 2(I):21–33.

Robinson PA, Gao X, Han Y. Relationships between lognormal distributions of neural properties, activity, criticality, and connectivity. Biological Cybernetics. 2021 Apr; 115(2):121–130. https://link.springer.com/10.1007/s00422-021-00871-z, doi: 10.1007/s00422-021-00871-z.

Santuy A, Rodríguez JR, DeFelipe J, Merchán-Pérez A. Study of the Size and Shape of Synapses in the Juvenile Rat Somatosensory Cortex with 3D Electron Microscopy. eNeuro. 2018; 5(1). https://www.eneuro.org/content/5/1/ENEURO.0377-17.2017, doi: 10.1523/ENEURO.0377-17.2017.

Schultz-Darken N, Braun KM, Emborg ME. Neurobehavioral development of common marmoset monkeys: Marmoset Neurobehavioral Development. Developmental Psychobiology. 2016 Mar; 58(2):141–158. https://onlinelibrary.wiley.com/doi/10.1002/dev.21360, doi: 10.1002/dev.21360.

Turner EC, Young NA, Reed JL, Collins CE, Flaherty DK, Gabi M, Kaas JH. Distributions of Cells and Neurons across the Cortical Sheet in Old World Macaques. Brain, Behavior and Evolution. 2016; 88(1):1–13. doi: 10.1159/000446762.

Van Kampen NG. Stochastic Processes in Physics and Chemistry. 3 ed. North Holland; 2007.

Wang SSH, Shultz JR, Burish MJ, Harrison KH, Hof PR, Towns LC, Wagers MW, Wyatt KD. Functional Trade-Offs in White Matter Axonal Scaling. Journal of Neuroscience. 2008; 28(15):4047–4056. https://www.jneurosci.org/content/28/15/4047, doi: 10.1523/JNEUROSCI.5559-05.2008.

Yurt KK, Kivrak EG, Altun G, Mohamed H, Ali F, Gasmalla HE, Kaplan S. A brief update on physical and optical disector applications and sectioning-staining methods in neuroscience. Journal of Chemical Neuroanatomy. 2018; 93:16–29. https://linkinghub.elsevier.com/retrieve/pii/S0891061817302831, doi: 10.1016/j.jchemneu.2018.02.009.

Supplementary tables

Table S1. Cortical areas included in this study.

Species	Area abbreviations
Mouse	FRP, MOp, MOs, SSp, SS-n, SSp-bfd, SSp-ll, SSp-m, SSp-ul, SS-tr, SSs, VISC, AUDd, AUDp, AUDpo, AUDv, VISal, VISam, VISl, VISp, VISpl, VISpm, ACAd, ACAv, ACAv, ACAv, ORBl, ORBm, ORBvl, AId, AIp, AIv, RSPagl, RSPd, RSPv, AONd, AONe, AONl, AONm, AONpv, TTd, TTv
Marmoset	A10, A9, A46V, A46D, A8aD, A8b, A8aV, A47L, A47M, A45, A47O, ProM, A11, A13b, A13a, A13L, A13M, OPAl, OPro, Gu, A32, A32V, A14R, A14C, A25, A24a, A24b, A24c, A24d, A6DR, A6Vb, A6Va, A8C, A6M, A6DC, A4c, A4ab, PaIM, AI, PaIL, DI, GI, IPro, TPro, S2PR, A3a, S2PV, A3b, S2I, S2E, A1-2, AuRTL, AuRT, AuRPB, AuRTM, AuR, AuRM, AuAL, AuA1, AuCM, AuCPB, AuML, AuCL, TPPro, STR, TE1, TPO, ReI, TE2, PGa-IPa, TPt, TE3, TEO, Pir, APir, Ent, A36, A35, TF, TL, TH, TLO, TFO, A23c, A23a, A29d, A30, A23b, A29a-c, A23V, ProSt, PF, PE, PFG, A31, AIP, PG, PEC, VIP, LIP, PGM, V6A, OPt, MIP, MST, FST, V5, V4T, A19M, V3A, V4, V6, A19DI, V3, V2, V1
Macaque_1	2, 5, 9, 10, 11, 12, 13, 14, 23, 25, 32, 24a, 24c, 24d, 46d, 46v, 7A, 7B, 7m, 8B, 8l, 8m, 8r, 9-46d, 9-46v, DP, ENTO, F1, F2, F3, F4, F5, F6, F7, LIP, MT, OPAI, OPRO, PERI, STPi, TEad, TEav, TEO, TH-TF, V1, V2, V3A, V4
Human	FA, FB, FC, FCBm, FD, FDΔ, FDt, FE, FF, FG, FH, FJ, FK, FL, FM, FN, LA1, LA2, LC1, LC2, LC3, LD, LE1, LE2, IA, IB, OA, OB, OC, PA, PB1, PB2, PC, PD, PE, PF, PG, PH, HA, HB, HC, HD, HE, HF, TA, TB, TC, TD, TE, TF, TG
Galago_1 & Owl Monkey	V1, V2, dV3, vV3, S1, M1, A1, MT, premotor, DL, Remain Ctx, Surr Ctx

Table S2. Results of the Shapiro-Wilk test for normality of $\ln(\rho_s)$ in marmoset cortical areas. Values rounded to two significant digits.

Area	S	p-value	Area	S	p-value	Area	S	p-value
V1	0.97	0.39	AI	0.98	0.96	TH	0.97	0.66
A10	0.95	0.19	PaIL	0.95	0.33	TLO	0.96	0.18
A9	0.98	0.51	DI	0.96	0.45	TFO	0.97	0.26
A46V	0.98	0.56	GI	0.97	0.67	A23c	0.97	0.36
A46D	0.98	0.49	Ipro	0.97	0.66	A23a	0.99	0.98
A8aD	0.97	0.34	TPro	0.97	0.77	A29d	0.95	0.21
A8b	0.96	0.16	S2PR	0.92	0.006	A30	0.98	0.73
A8aV	0.96	0.17	A3a	0.95	0.04	A23b	0.97	0.45
A47L	0.96	0.052	S2PV	0.93	0.014	A29a-c	0.97	0.7
A47M	0.97	0.3	A3b	0.96	0.2	A23V	0.96	0.15
A45	0.96	0.18	S2I	0.97	0.33	ProSt	0.93	0.018
A47O	0.98	0.7	S2E	0.94	0.0046	PF	0.93	0.012
ProM	0.97	0.21	Area1-2	0.97	0.37	PE	0.94	0.03
A11	0.97	0.41	AuRTL	0.97	0.4	PFG	0.92	0.0046
A13b	0.96	0.58	AuRT	0.95	0.039	A31	0.97	0.31
A13a	0.91	0.048	AuRPB	0.98	0.89	AIP	0.96	0.063
A13L	0.97	0.45	AuRTM	0.97	0.73	PG	0.91	0.002
A13M	0.99	0.97	AuR	0.97	0.48	PEC	0.91	0.0032
OPAI	0.99	0.99	AuRM	0.9	0.017	VIP	0.92	0.0044
OPro	0.98	0.75	AuAL	0.94	0.12	LIP	0.95	0.042
GU	0.95	0.058	AuA1	0.98	0.48	PGM	0.98	0.78
A32	0.96	0.24	AuCM	0.97	0.33	V6A	0.95	0.068
A32V	0.96	0.51	AuCPB	0.93	0.037	OPt	0.91	0.0015
A14R	0.98	0.77	AuML	0.97	0.44	MIP	0.9	0.00091
A14C	0.79	5.5e-06	AuCL	0.94	0.045	MST	0.98	0.53
A25	0.89	0.022	TPPro	0.98	0.91	FST	0.95	0.1
A24a	0.96	0.35	STR	0.96	0.44	V5	0.98	0.68
A24b	0.97	0.41	TE1	0.96	0.17	V4T	0.95	0.082
A24c	0.97	0.54	TPO	0.97	0.31	A19M	0.98	0.8
A24d	0.92	0.017	ReI	0.95	0.4	V3A	0.91	0.006
A6DR	0.97	0.23	TE2	0.96	0.15	V4	0.98	0.61
A6Vb	0.97	0.32	PGa/IPa	0.97	0.45	V6	0.94	0.048
A6Va	0.98	0.56	TPt	0.94	0.033	A19DI	0.95	0.074
A8C	0.95	0.055	TE3	0.93	0.026	V3	0.97	0.53
A6M	0.99	0.98	TEO	0.95	0.087	V2	0.96	0.29
A6DC	0.91	0.002	A36	0.98	0.54	Ent	0.99	0.99
A4c	0.97	0.43	A35	0.97	0.31	APir	0.94	0.24
A4ab	0.96	0.076	TF	0.95	0.11	Pir	0.93	0.21
PaIM	0.93	0.2	TL	0.95	0.096			

Supplementary figures

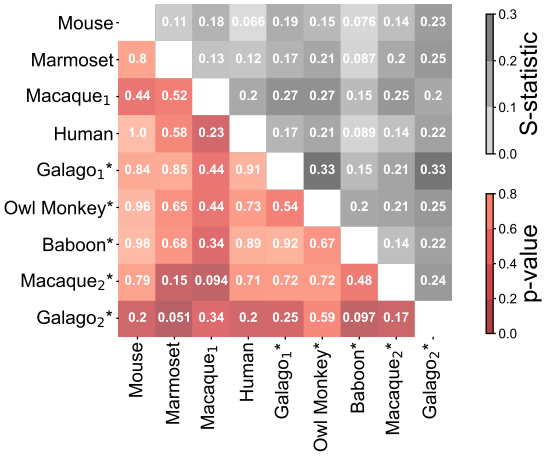

Figure 1-Figure supplement 1. Pairwise Kolmogorov-Smirnov two-sample two-sided tests. P-values and S-statistics displayed below and above the diagonal, respectively. The z-scored log neuron density distributions of the four species are statistically indistinguishable at the 0.05 level.

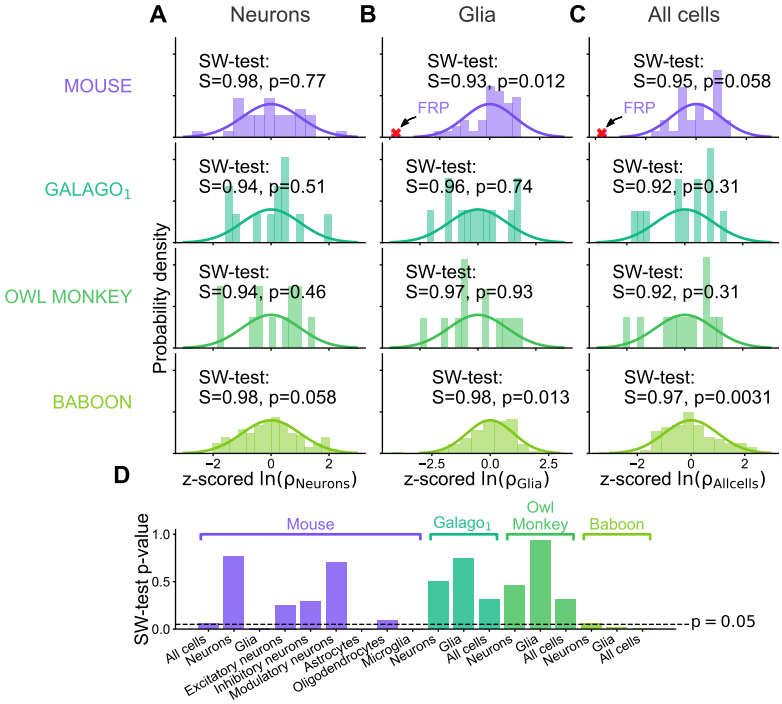

Figure 1-Figure supplement 2. Comparison of neuron and glia lognormality. A–C Histogram of z-scored log density and result of Shapiro-Wilk test for neurons (**A**), glia (**B**), and all cells combined (**C**). **D** Barplot of p-values resulting from Shapiro-Wilk normality test for all cell types. Panel **A** is equivalent to the data shown in ***Figure 1***.

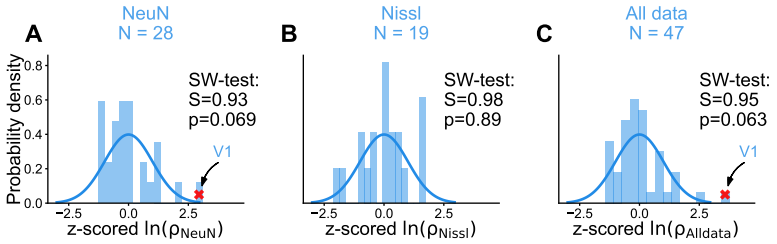

Figure 1-Figure supplement 3. Lognormality of cell densities from different staining types in macaque cortex based on the macaque$_1$ data set. A-C Histogram of z-scored log density and result of Shapiro-Wilk test for NeuN staining only (**A**), Nissl staining only (**B**) and all measurements combined (**C**). The Nissl data were scaled down based on the linear relationship with the NeuN data (***Beul and Hilgetag, 2019***). Red crosses indicate outliers (|z-scored $\ln(\rho)| \geq 3$, which were excluded from the test. Panel **C** is equivalent to the data shown in ***Figure 1***.

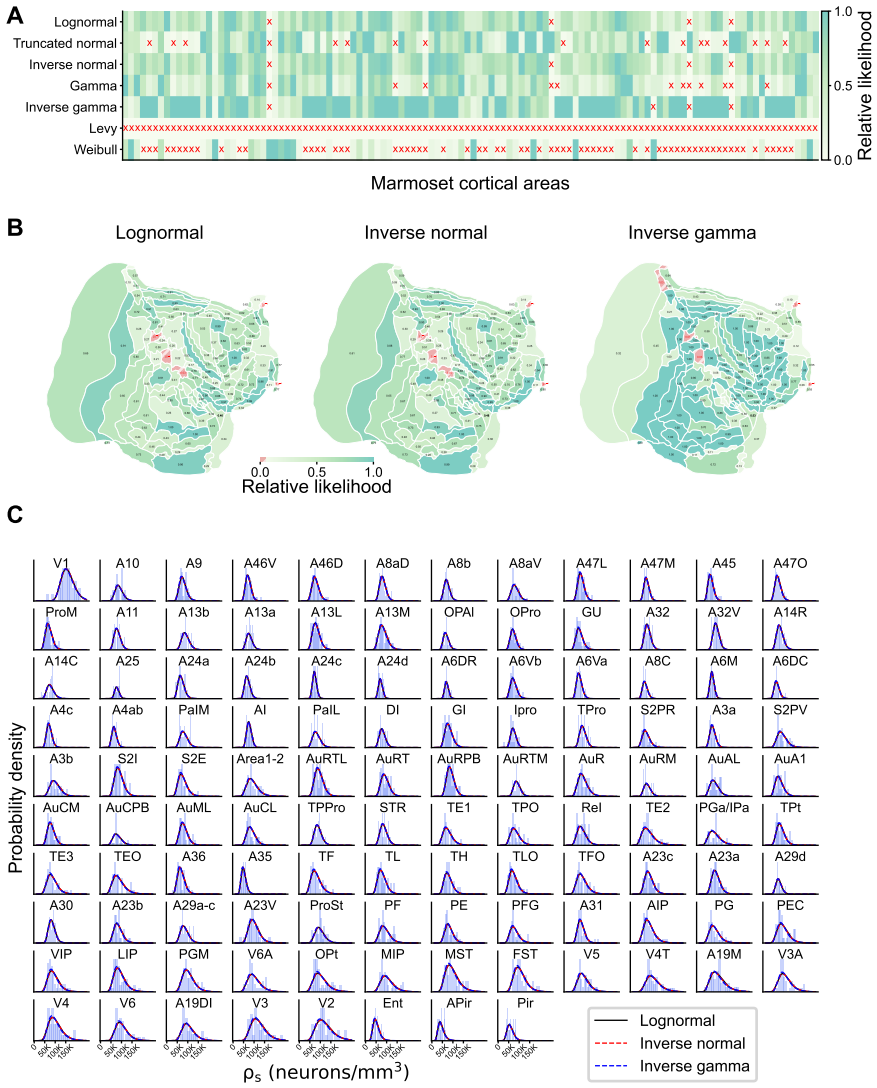

Figure 3-Figure supplement 1. Statistical model comparison within the marmoset cortical areas. A Relative likelihood for seven compatible statistical models for all areas of the marmoset; a red cross (x) indicates a relative likelihood < 0.05 with respect to the model with the highest likelihood. **B** Spatial distribution of relative likelihood for the three best statistical models. **C** The three best statistical models fitted to the neuron density histograms in each area of marmoset cortex; the three models produce visually nearly indistinguishable fits.

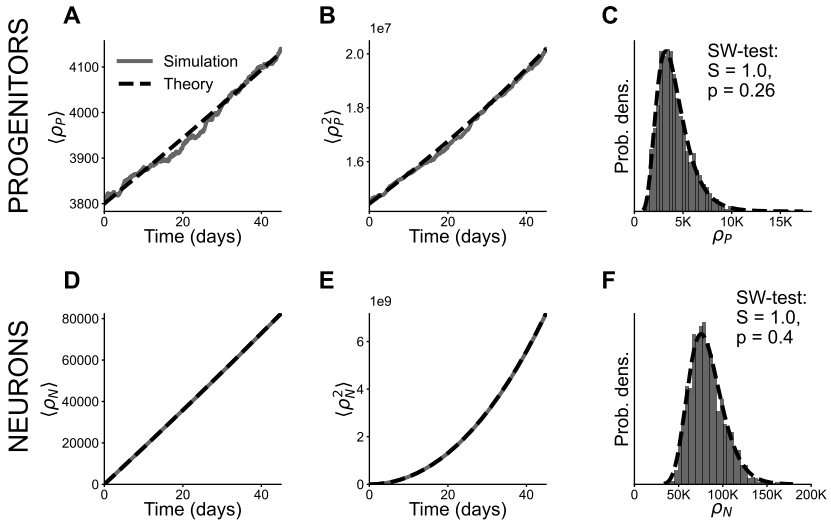

Figure 4-Figure supplement 1. Verification of neurogenesis model. A, B, D, E Time evolution of the mean density of progenitors (A) and neurons (D) and the corresponding second moment for progenitors (B) and neurons (E). Theory based on Equations (8) and (10). **C, F** Resulting progenitor (C) and neuron (F) density distributions at the end of neurogenesis. Both distributions are compatible with a lognormal; for the neuron density this is not a formal result but rather an approximation based on Equation (11). Simulation parameters: time step $\Delta t = 0.05\,\text{days}$, total time $T = 45\,\text{days}$, $N_{\text{sample}} = 2000$ samples, initial progenitor density $\rho_0 = 3.8 \times 10^3$, average rate $\lambda = 2\log(2)/3\,\text{days}$, and noise intensity $\sigma = 0.061\,\text{days}^{-1/2}$.